Efficient n⁺p-Si photocathodes for solar H_2 production catalyzed by Co-W-S and stabilized by Ti buffer layer

Ronglei Fan[a,b], Guanping Huang[a], Yongjie Wang[b], Zetian Mi[b], Mingrong Shen[a,*]

[a] College of Physics, Optoelectronics and Energy, Jiangsu Key Laboratory of Thin Films, Collaborative Innovation Center of Suzhou Nano Science and Technology, Soochow University, 1 Shizi Street, Suzhou, 215006, China
[b] Department of Electrical Engineering and Computer Science, Center for Photonics and Multiscale Nanomaterials, University of Michigan, 1301 Beal Avenue, Ann Arbor, MI, 48109, United States

ABSTRACT

Photoelectrochemical (PEC) water splitting is regarded as a promising route to produce sustainable hydrogen fuel using sunlight and water as sole inputs. Si is one of the most promising potential materials for PEC photocathode, while developing highly active non-precious catalysts and stable semiconductor/catalyst interface is critical to bring solar water splitting into reality. Herein, we reported a cheap and effective strategy based on a wet chemical method to integrate WS_2 and Co-doped WS_2 (Co-W-S) onto n⁺p-Si as noble metal−free catalysts for H_2 production. Co-W-S/n⁺p-Si photocathode exhibited much better PEC performance, resulting from the Co-W-S catalyst which has more electrochemically active sites and better electrical conductivity. A thin Ti interlayer between Co-W-S and Si was inserted to further optimize the PEC performance, especially the stability of the photocathode. As a result, an onset potential of 0.36 V *vs.* RHE, a photocurrent of 30.4 mA/cm² at 0 V *vs.* RHE and an energy conversion efficiency of 4.0% were obtained under simulated AM1.5 G illumination, along with a long-term stability for 6 days of continuous PEC reaction.

1. Introduction

Solar water splitting using photoelectrochemical (PEC) cells, a promising approach to convert intermittent solar energy into storable energy carrier hydrogen, is gaining broad and increasing attention to cope with the global energy crisis and environmental issues [1,2]. The semiconductor photoelectrodes in PEC cells must absorb a large portion of the solar spectrum, have fast H_2 or O_2 evolution kinetics to facilitate charge transfer and to reduce the overpotential for H_2 or O_2 production, and maintain long term stability under operating conditions [3,4]. Si, a basic material of electronic industry and photovoltaics, is earth-abundant and low cost. Its bandgap (1.12 eV) is beneficial to absorb sunlight and its theoretical maximum photocurrent can reach up to 44 mA cm² under AM1.5 G one Sun illumination. Recently, Si has also been widely employed in PEC systems as the photocathode since the position of its conduction band edge is more negative than that of the potential of hydrogen evolution reaction (HER) during water splitting [5–8]. However, Si surface has to be catalyzed due to its slow intrinsic HER kinetics, and be protected to avoid the formation of insulating SiO_2 layer. Though Pt-group metals are the most outstanding HER catalysts, their prohibitive scarcity and cost hinders the widespread practical

application [9,10]. Thus, development of cheap but efficient and scalable materials for HER is highly important, while it is of equal importance to solve simultaneously the stability problem of Si photocathode.

Recently, significant progress has been made in two-dimensional (2D) materials, *e.g.* transition metal dichalcogenides (TMDs) [11–13]. Among them, tungsten disulfide (WS_2) has been identified as a new class of catalyst for electrochemical HER [14]. Similar to MoS_2 and other TMDs, WS_2 is a layered structure material composed of individual sandwiched S-W-S layers. Bulk WS_2 material is a poor electrochemical catalyst because the exposed basal planes are HER inert, while its edge sites show highly catalytic activity [15]. Different synthetic approaches have been explored to synthesize WS_2 catalyst [16–18], wherein wet chemical method based on the pyrolysis of ammonium tetrathiotungstate ($(NH4)_2WS_4$) is a cheap and scalable approach [19]. In order to increase the edge sites and thereby improve the HER activity, various engineering approaches have been investigated. Doping foreign atoms into TMDs to form ternary structures seems to play a pivotal role. These foreign atoms included non-metal atoms such as selenium [16], carbon [20], and phosphorus [21]. It has also currently been observed that the bimetallic catalyst systems exhibit better performance than
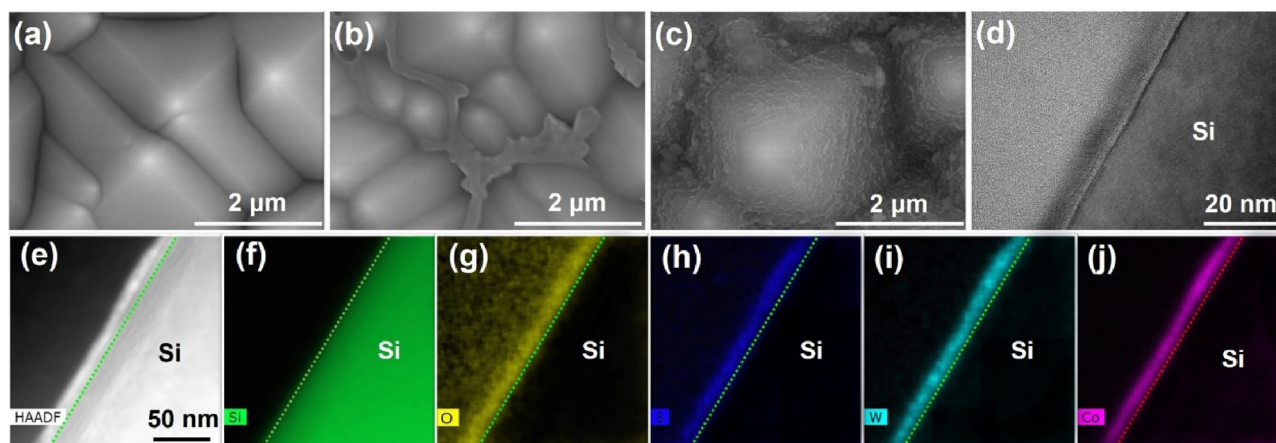
Fig. 1. Top-down SEM images of (a) n^+p-Si, (b) WS_2/n^+p-Si, (c) Co-W-S/n^+p-Si. (d) Cross-sectional TEM micrograph and (e) HAADF-STEM image of as-synthesized Co-W-S/n^+p-Si sample. EDS elemental mappings of Co-W-S/n^+p-Si sample: (f) Si, (g) oxygen, (h) sulfur, (i) tungsten and (j) cobalt.

their individual metal counterparts, thanks to the enhanced conductivity, formation of structural defects, and/or increment in electrochemically active sites [22]. Previously, Shang et al. reported that the formation of a bimetallic structure *via* the doping of Co, Fe and Ni ions into WS_2 can promote the electrocatalytic activity of the pure WS_2, and the best performance of -190 mV_{RHE} (RHE: reversible hydrogen electrode; V_{RHE}: V *vs.* RHE) at 10 mA/cm^2 was obtained [17].To date, however, most of such studies have only been exploited as electrocatalysts for HER and few works tried to integrate WS_2 based bimetallic catalysts onto Si photocathodes for PEC-HER where both efficient catalysis and stability are required.

It is highly challenging to integrate catalysts with light absorbers, due to the following two issues. The first is the synthetic difficulties such as the uniform morphology and coverage of catalysts on light absorbers, while the second is related to the semiconductor/catalyst chemical incompatibility, leading to interfacial recombination sites and/or stability issues [23]. Till now, several works for TMDs integrated n^+p-Si photocathodes have been reported, wherein the built-in n^+p junction is independent of the semiconductor/liquid junction, and can provide a high onset potential (V_{on}) relative to a p-Si photocathode. Specifically, Seger et al. electrodeposited amorphous MoS_x on Ti-protected n^+p-Si photocathode. 0.33 V_{RHE} V_{on} and 16 mA/cm^2 J_0 (J_0: photocurrent density at 0 V_{RHE}) were obtained under AM1.5 cutoff (< 635 nm) and intensity of 38.6 mW/cm^2, and 1 h stability was proved [24]. Cabán-Acevedo et al. integrated CoPS on n^+p-Si photocathode, achieving a J_0 of 26 mA/cm^2 and V_{on} of 0.44 V_{RHE} under simulated 1 Sun irradiation (100 mW/cm^2), while its stability was not reported [25]. By loading nano-particulate CoP catalyst on radial-junction n^+p-Si microwire arrays, Roske et al. showed a saturated photocurrent density of 17 mA/cm^2, V_{on} of 0.48 V_{RHE} and 12 h stability [26]. By integrating the MoS_xCl_y catalyst with n^+p-Si micro-pyramids, Ding et al. achieved a high J_0 of 43 mA/cm^2, V_{on} of 0.41 V_{RHE} and 2 h stability [4]. Using a thin Mo/MoS_2 protecting interlayer and $[Mo_3S_{13}]^{2-}$ nanoclusters as surface catalyst, Benck et al. showed an 0.4 V_{RHE} V_{on}, 17.5 mA/cm^2 J_0 and 100 h stability for the n^+p-Si photocathode [7]. However, the protective layer seems to inhibit the light absorption of Si and only 17.5 mA/cm^2 J_0 was reported. Our group has recently demonstrated a highly efficient and stable photocathode by sputtering a MoS_2 layer catalyst onto n^+p-Si surface with a ~ 2 nm Al_2O_3 interlayer. 0.4 V_{RHE} V_{on} and 35.6 mA/cm^2 J_0 was achieved, but the fill factor (FF) is limited to 0.28 due to the increased resistance on the interfaces of MoS_2/Al_2O_3/n^+p-Si and thus the energy conversion efficiency (η) is limited to 3.6% [13]. Despite the progress made, few works have simultaneously achieved both high efficiency and long-term stability. Two problems need to be solved simultaneously: (1) The catalyst and protective layers should be thin enough to avoid shielding the sunlight

on Si; (2) The protective layer should be conductive to connect the Si and catalyst efficiently.

In this study, we firstly use a cheap wet chemical method to integrate thin WS_2 and Co doped WS_2 (Co-W-S) layers onto n^+p-Si to study the Co doping effect on the PEC reactivity of the photocathodes, aiming for high η. Secondly, we try to insert a thin Ti interlayer between Co-W-S and Si to optimize the PEC performance, especially the stability of the photocathode. Conformal and bimetallic Co-W-S catalyst was successfully fabricated on Ti buffered n^+p-Si surface. A V_{on} of 0.36 V_{RHE}, J_0 of 30.4 mA/cm^2 and a η of 4.0% were obtained under simulated AM1.5 G illumination (100 mW/cm^2). In addition, the electrode exhibited long-term stability under 6 days of continuous PEC-HER operating conditions. This strategy offers a cheap and effective synthesis of Co-W-S catalyst on Ti/n^+p-Si photocathode which provides an alternative for Pt catalyst in PEC-HER.

2. Results and discussion

Detailed experimental procedures of the n^+p-Si electrodes are provided in the experimental section. Briefly, micro-pyramids structure was firstly fabricated on planar p-type Si wafers by KOH etching in order to improve the light-harvesting ability and the interfacial area. Then, an n^+p surface junction was fabricated onto the p-type Si. Structural properties of these electrodes are characterized using scanning electron microscopy (SEM) and transmission electron microscopy (TEM). Fig. 1a shows the top-down SEM image of the n^+p-Si electrode with surface micro-pyramid texture of ~ 2 μm in depth. The precursor solution containing $(NH4)_2WS_4$ was spin-coated onto the n^+p-Si substrate. After drying under ambient conditions for several minutes, the coated n^+p-Si substrate was moved into a furnace for thermal treatment at 400 °C for 2 h under nitrogen flow to decompose $(NH4)_2WS_4$. This sample is defined as WS_2/n^+p-Si. The SEM in Fig. 1b shows that WS_2 clusters with dendritic-like morphologies are located at the bottom of the pyramid texture. This result is in agreement with a previous report about the synthesis of fullerene-like WS_2 [27]. The addition of $CoCl_2$ into $(NH4)_2WS_4$ precursor solution can make the morphology different, as shown in Fig. 1c. The surface of n^+p-Si is uniformly covered by Co-W-S catalyst layer. The different growth modes for WS_2 and Co-W-S on Si can be originated from the different hydrophily of the precursor $(NH4)_2WS_4$ and $CoCl_2$ doped $(NH4)_2WS_4$ solutions on Si. This is confirmed by the corresponding testing that the contact angle of $(NH4)_2WS_4$ solution on n^+p-Si sharply decrease from 50.3° to 3.1° after the adding of $CoCl_2$ (Fig. S1), illustrating that the homogeneous distribution of $CoCl_2$ doped $(NH4)_2WS_4$ solution forms on Si surface before drying, resulting in the uniform growth of Co-W-S on Si.

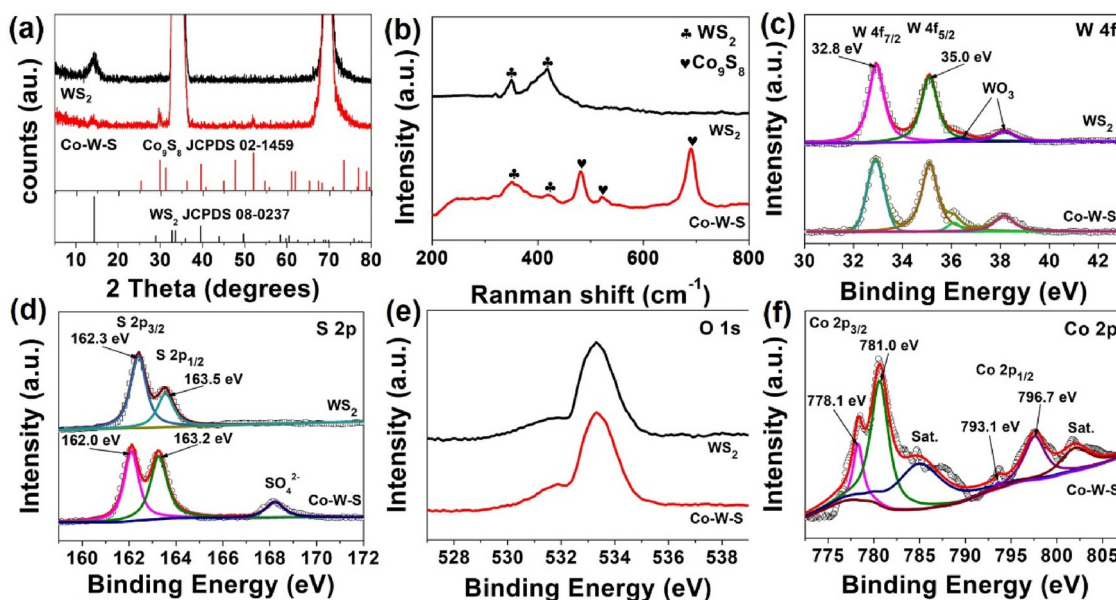Cross-sectional TEM shown in Fig. 1d again reveals a conformal thin

Fig. 2. XRD pattern (a) and Raman spectra (b) of WS_2/n^+p-Si and Co-W-S/n^+p-Si. High-resolution XPS of (c) W 4f, (d) S 2p, (e) O 1 s and (f) Co 2p in WS_2/n^+p-Si and/or Co-W-S/n^+p-Si.

layer with a thickness about 8 nm covering the sample surface. Lattice fringes of Co-W-S are indiscernible in the high-resolution images, suggesting its poor crystallinity. In order to characterize the interface of Co-W-S/n^+p-Si more clearly, high-angle annular dark-field scanning TEM (HAADF-STEM) image and corresponding energy dispersive spectrometer (EDS) elemental mappings are conducted (Fig. 1e–j). Three dominating components (S, W, and Co), with a small amount of O, make up the obtained material, showing the homogeneous distribution over the layer. STEM-EDS mappings also indicate that no SiO_2 layer is formed between the n^+p-Si and Co-W-S catalyst, implying that the Co-W-S catalyst layer establishes an intimate contact with Si. This is very important to keep the photocathode functional. It is evident from Fig. 1 that a uniformly distributed Co-W-S catalyst layer can be successfully fabricated on the n^+p-Si surface without an interfacial SiO_2 layer.

To explore the crystal structure and crystallinity of the WS_2 and Co-W-S catalysts, X-ray diffraction (XRD) pattern measurements are taken. In Fig. 2a, the two strong peaks located at approximately 2θ value of 33 and 69°are ascribed to the underlying n^+p-Si [28]. WS_2/n^+p-Si sample shows a broad diffraction peak at 2θ value of 14.3°, which corresponds to the (002) plane of hexagonal WS_2 (JCPDS 08-0237). However, this peak becomes weak after the incorporation of Co atoms. In addition, Co-W-S/n^+p-Si exhibits two additional weak peaks at 2θ value of 29.7 and 51.9°, matching well with the (311) and (440) planes of Co_9S_8 (JCPDS 02-1459). Raman spectroscopy (Fig. 2b) was made to further confirm the formation of desired materials. Two peaks at 353 and 421 cm^{-1} for WS_2/n^+p-Si are due to E_{2g}^1 (in-plane) and A_{1g} (out of plane) phonon vibration modes in WS_2, respectively, consistent with those found in WS_2 synthesized by sulfurization reaction of WO_3 [20]. For Co-W-S/n^+p-Si, there are other peaks at 481, 520 and 691 cm^{-1}, in agreement with the ones observed in Co_9S_8 [29]. Noting that in order to get clear composition and crystallographic structure of the WS_2 and Co-W-S coatings, we prepared specially thick WS_2 and Co-W-S films on n^+p-Si before the XRD and Raman measurements, and therefore the Raman information for Si can't be observed.

In order to gain insight into the surface chemical states in WS_2 and Co-W-S films, X-ray photoelectron spectroscopy (XPS) analysis was conducted, as shown in Fig. 2c–f. W4f spectra of WS_2/n^+p-Si and Co-W-S/n^+p-Si are almost the same (Fig. 2c). The peaks of W^{4+} $4f_{7/2}$ and W^{4+} $4f_{5/2}$ appear at the binding energy (BE) of 32.8 and 35.0 eV,

consistent with previous reports [30,31]. A weak doublet at 35.92 and 38.05 eV likely originates from the small surface oxidation. In Fig. 2d, the S 2p spectrum of WS_2/n^+p-Si shows $2p_{3/2}$ and $2p_{1/2}$ peaks at 162.3 and 163.5 eV, respectively, arising from WS_2 [30,31]. They slightly shift to lower binding energies in Co-W-S (162 and 163.2 eV). According to the report of Feng et al., the S 2p peaks at 161.5 and 162.5 eV are attributed to the $2p_{3/2}$ and $2p_{1/2}$ core levels in Co_9S_8, respectively [29]. Therefore, the peaks for Co-W-S are between those of WS_2 and Co_9S_8. The weak peak identified in the high binding energy region (168.7 eV) in Fig. 2d was assigned to the oxidized S species, labeled as SO_4^{2-}, indicating the presence of some sulfate/sulfite moieties in the materials due to the possible partial oxidation of S [32]. The O 1s peak of WS_2/n^+p-Si remains unchanged after the incorporation of Co, as shown in Fig. 2e. For Co 2p spectrum in Fig. 2f, the intensive peaks at 778.1 and 781.0 eV, 793.1 and 796.7 eV are assigned to a spin-orbit splitting value of Co 2p3/2 and Co 2p1/2, respectively, accompanied by two satellite peaks. This agrees with the previous report and again manifests the formation of Co_9S_8 [33,34]. By integrating all of the characterization results together we conclude that the Co atoms join in Co_9S_8 which coexists with WS_2 in Co-W-S. As will be demonstrated below, such a Co-W-S hybrid can be a promising and superior catalyst for the PEC-HER.

PEC activity during water splitting was assessed by recording the photocurrent density *vs.* potential (*J–V*) curves at 50 mV/s in 1 M $HClO_4$ solution (pH = 0.3) in the dark and under simulated AM1.5 G illumination (100 mW/cm^2). We defined the onset potential V_{on} of the *J–V* curve which drives the photocurrent density to -1 mA/cm^2. In Fig. 3a, no current is observed for all the electrodes under dark conditions. For the bare n^+p-Si photocathode, the photocurrent increases gradually from -1 to -36 mA/cm^2 when V_{RHE} changes from about -0.2 to -1.2 V_{RHE}, consistent with our previous studies [8,13]. When the WS_2 is coated on the electrode surface, the *J–V* curve shifts right obviously. The PEC activity of the WS_2/n^+p-Si photocathodes is controlled by the number of deposition cycles (Fig. S2). Among these samples, the photocathode with 2 deposition cycles exhibits the best performance: V_{on} of 0.18 V_{RHE} and a J_0 of -6.5 mA/cm^2. In addition, we also checked that the 400 °C annealing for WS_2 is the best temperature for the PEC performance of the WS_2/n^+p-Si photocathodes (Fig. S3). On this basis, Co-W-S is fabricated on n^+p-Si. Fig. 3a reveals that the resulting Co-W-S/n^+p-Si photocathode has much better PEC performance: J_0 increases by
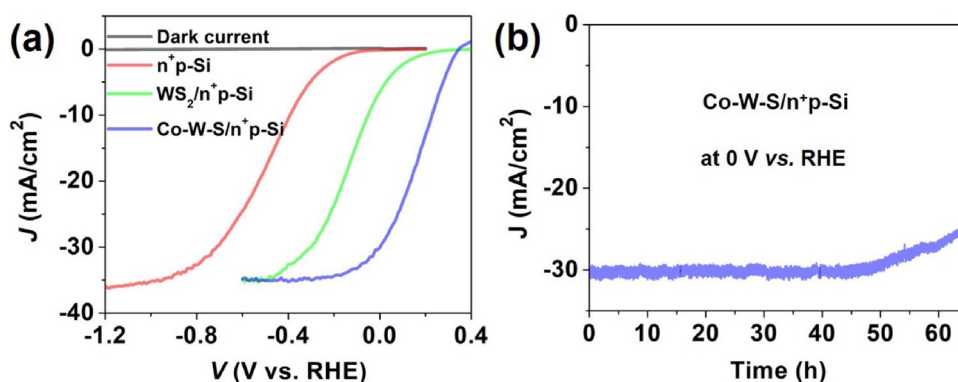
Fig. 3. (a) PEC J–V curves of the bare n^+p-Si, WS_2/n^+p-Si and Co-W-S/n^+p-Si photocathodes. (b) PEC stability measurement for the Co-W-S/n^+p-Si electrode during solar H_2 generation.

a factor of 4.6, from -6.5 to $-30.1\,mA/cm^2$, while V_{on} shifts more right from 0.18 to $0.32\,V_{RHE}$. The effect of Co concentration was also studied. Remarkably, the Co-W-S catalyst with the molar ratio of Co/W (1:1) in the initial solution exhibits the best HER activity (Fig. S4). When the molar ratio of Co/W in the initial solution increases from 1:1 to 2:1, the corresponding Co-W-S/n^+p-Si photocathode does not exhibit better HER activity, indicating the high performance of Co-W-S is not simply due to the introduction of Co_9S_8. Generally, Co_9S_8 exhibits poorer electrochemical performance for HER but relatively higher electrical conductivity than MoS_2 due to its sluggish ion transport kinetics [29]. In this respect, Zhu et al. designed $Co_9S_8@MoS_2$ core–shell /carbon nanofibers ($Co_9S_8@MoS_2$/CNFs) hybrid system, which exhibits impressive enhanced HER activities compared to pure MoS_2/CNFs and Co_9S_8/CNFs nanostructures due to the synergetic effects between Co and Mo at the proposed localized interface region between the MoS_2 and Co_9S_8 phases [32]. We believe that the synergetic effects can also be suitable for the WS_2 and Co_9S_8 in the synthetic Co-W-S catalyst.

Despite the enhancement in J_0, the saturated photocurrent density for WS_2 and Co-W-S catalyzed n^+p-Si reduces a little from -36 to $-35\,mA/cm^2$ when compared with the pure n^+p-Si. This may be due to the slight light absorption by the catalyst. To check this point, the optical properties are explored. The reflectance of WS_2/n^+p-Si and Co-W-S/n^+p-Si photocathodes are nearly the same with that of bare n^+p-Si, indicating that the thin WS_2 and Co-W-S layers do not obviously affect the light intensity obtained by Si (Fig. S5a). However, the WS_2 and Co-W-S layers both have an absorption of $\sim 2.7\%$ in the 300–900 nm wavelength region, by comparing the UV–vis transmittance spectra of transparent indium tin oxide (ITO) coated glass substrates before and after the decoration of WS_2 and Co-W-S layers (Fig. S5b). These results are consistent with the $\sim 2.7\%$ decrease in saturated photocurrent density, since the photogenerated carriers in Si are proportional to the light intensity shining on Si, which determines the saturated photocurrent [35].

Fig. 3b displays the stability of the Co-W-S/n^+p-Si electrode in 1 M $HClO_4$ solution under simulated AM1.5 G illumination ($100\,mW/cm^2$) during H_2 evolution. Under potentiostatic control at $0\,V_{RHE}$, the current density is stable at $30 \pm 1\,mA/cm^2$ for about 45 h. However, it begins to drop after 45 h of continuous operation, indicating the inferior stability of the photocathode. The reasons for the poor stability of Co-W-S/n^+p-Si may include catalyst detachment, catalyst deactivation, and reduced quality of the contact between catalyst and Si substrate. (1) Comparing with the SEM image before the PEC-HER test, the one taken after 65 h stability measurement (Fig. S6) shows that the Co-W-S surface morphology does not change, indicating Co-W-S still adheres to Si and its detachment does not become an issue over such long-time period. (2) We will also show in the following that the catalyst does not deactivate during the 7-day continuous electrochemical HER reaction. (3) In order to illustrate the change of interface between catalyst and Si

substrate, HAADF-STEM image and EDS elemental mappings of Co-W-S/n^+p-Si sample after the 65 h continuous PEC-HER was conducted. As shown in Fig. S7, an amorphous interfacial SiO_2 layer with a thickness of $\sim 5\,nm$ arises between Si and Co-W-S. According to the previous study reported by Seger et al., n^+p-Si electrode with a thin SiO_2 layer (above 2 nm) can form a 3.1 eV barrier that severely limits electron transport [24]. Therefore, additional strategies must be proposed to solve the interface problem for practical applications.

To study the catalytic performance of the as-prepared WS_2 and Co-W-S catalysts, we deposited them on the carbon fiber (CF) substrates and measured their electrochemical characteristics *via* a standard three-electrode configuration in 1 M $HClO_4$ solution. The synthesis conditions were the same as those on Si substrate except changing their amount to optimize the catalytic performance (Fig. S8). Fig. 4a summarizes the J–V curves with iR correction for the best performing WS_2 and Co-W-S in comparison with the 20% Pt/C and blank *CF*. The blank CF shows negligible current density between $–0.5$ and $0.1\,V_{RHE}$, indicating its poor catalytic performance. The WS_2 has an overpotential of $–340\,mV_{RHE}$ to reach the cathodic current density of $-10\,mA/cm^2$, consistent with the previous report [20]. The Co-W-S exhibits much better HER activity than WS_2, as demonstrated by a small overpotential of $-165\,mV_{RHE}$ at $-10\,mA/cm^2$. Furthermore, the corresponding Tafel slope (Fig. 4b) of 63 mV per decade for Co-W-S catalyst is also much smaller than that of WS_2 (97 mV per decade), suggesting a two-electron transfer process following Volmer–Heyrovsky mechanism of bimolecular adsorption and hydrogen evolution [36]. Such electrocatalytic activity is among the best performance of various WS_2-based catalysts [15,20,21,31,37].

Numerous studies have shown that Co doping in TMDs can intrigue their intrinsic catalytic activity through generating more active sites due to the increase of defects [17,38,39]. In addition, the SEM images in Fig. S9 reveal that Co-W-S on CF has larger effective electrochemical area with smaller particles than WS_2, similar to the observation in Fig. 1b and c when they are deposited on Si, respectively. Recently, Co_9S_8 has been studied as an attractive candidate for cheap HER electrocatalyst [32,40,41]. Similar to the WS_2, Co_9S_8 is also a transition metal sulfide, which, however, has higher electrical conductivity than WS_2. Therefore Co-W-S may also have improved conductivity. To check this point, the electrochemical impedance spectroscopy (EIS) were measured in 1 M $HClO_4$ electrolyte at an overpotential of $-165\,mV_{RHE}$ (Fig. 4c and Fig. S10). The simplified equivalent circuit is shown in the inset of Fig. 4c. The charge transfer resistance R_{ct} from CF to electrolyte through the Co-W-S catalyst is around $4.2\,\Omega$, while that for WS_2 is much larger as $\sim 86.7\,\Omega$. These results illustrate that Co incorporation can significantly improve the R_{ct}. This can be originated from the improved conductance and catalytic activity. The Co-W-S catalyst on CF substrate also shows an outstanding long-term stability. There is no loss in current at $-0.2\,V_{RHE}$ for about 7 days during H_2 evolution. Obviously, the
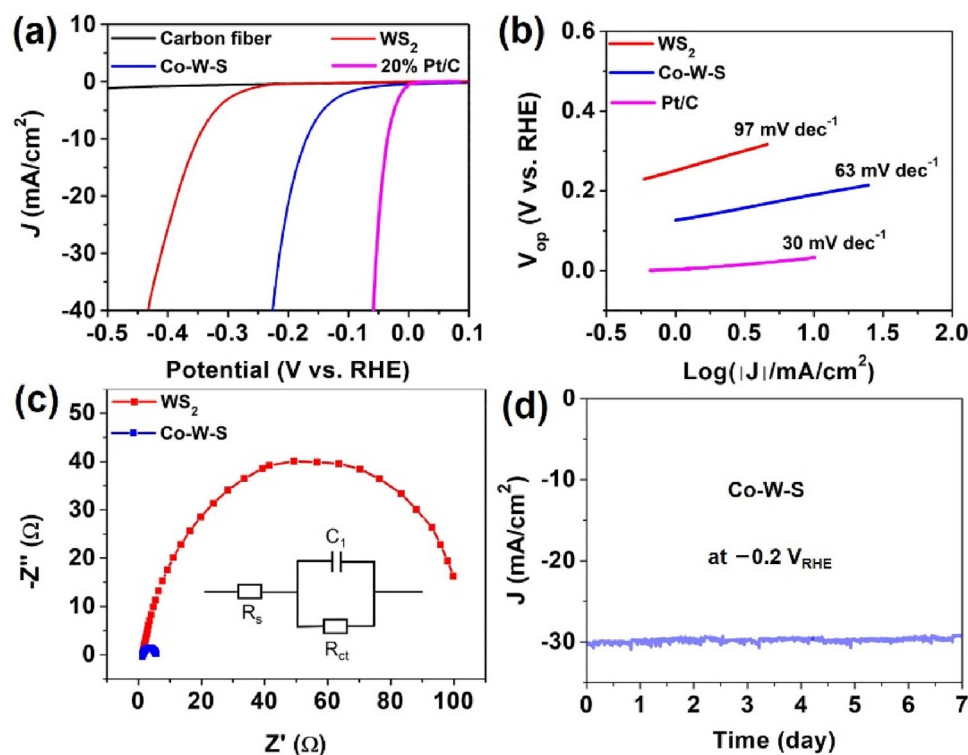
Fig. 4. Electrochemical characterization of WS$_2$ and Co-W-S catalysts prepared on CF substrates for HER catalysis. (a) *J–V* curves with *iR* correction of WS$_2$ and Co-W-S catalysts in comparison with those of 20% Pt/C and blank *CF*. (b) The Tafel slopes of WS$_2$, Co-W-S and 20% Pt/C obtained from the *J–V* curves in (a). (c) EIS of WS$_2$ and Co-W-S catalysts. Inset: the equivalent circuit corresponding to the charge transfer from the CF to the electrolyte through a catalyst. (d) Stability measurement for Co-W-S catalyst loaded on CF at −0.2 V$_{RHE}$.
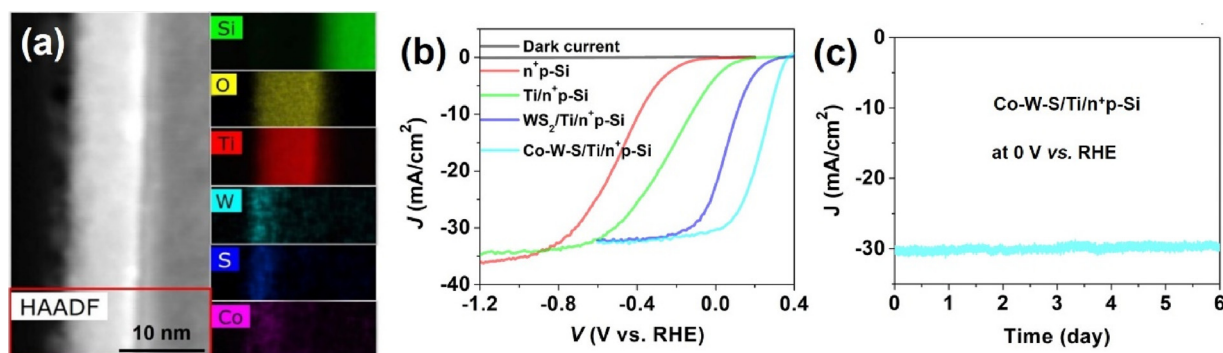

Fig. 5. (a) HAADF-STEM image and selective EDS elemental mappings of as-synthesized Co-W-S/Ti/n$^+$p-Si photocathode. (b) PEC *J–V* curves of n$^+$p-Si photocathodes with and without WS$_2$ and Co-W-S catalyst layer and/or 8 nm Ti buffer layer. (b) PEC stability measurement for the Co-W-S/Ti/n$^+$p-Si electrode during solar H$_2$ generation.

Co-W-S catalyst itself will not be deactivated in the HER operation condition (Fig. 4d). This point further verifies that the poor stability of Co-W-S/n$^+$p-Si is due to the formation of SiO$_2$ on the interface. Accordingly, we need to isolate Si from Co-W-S. To resolve the stability problem of Co-W-S/n$^+$p-Si, an ~8 nm Ti layer was deposited onto n$^+$p-Si by electron beam evaporation (E-beam), to form an ohmic contact between Co-W-S and n$^+$-Si. We defined this sample as Ti/n$^+$p-Si. Then we used Ti/n$^+$p-Si as substrate to replicate the same catalyst layer as n$^+$p-Si did. The SEM images in Fig. S11 show that the Ti layer does not affect the morphology of n$^+$p-Si or the distribution of the catalyst. Fig. 5a shows the HAADF-STEM image and selective EDS elemental mappings of the as-synthesized Co-W-S/Ti/n$^+$p-Si photocathode. The uniform color contrast for the six elements of Si, O, Ti, W, S and Co is observed, proving the uniformity of Ti buffer layer and Co-W-S catalyst on Si substrate. We note that the interfacial Ti buffer layer can be oxidized to TiO$_x$ after the on-surface synthesis of catalyst is carried out. However, no interfacial SiO$_2$ layer is observed owing to the protection of Ti buffer layer. Note TiO$_x$ is also conductive as proved by other groups [42,43], so it may also work as the efficient protective layer to connect Si and catalyst. Fig. 5b shows the *J–V* curves of the different

photocathodes with the Ti buffer layer. After coating the Ti layer on n$^+$p-Si, its V$_{on}$ shifts right obviously from –0.2 V to 0.08 V$_{RHE}$, due to the passivation role of TiO$_x$ on Si surface. The saturated photocurrent, however, decreases a little from –36 to –34.8 mA/cm^2 because of the possible light absorption by Ti buffer layer. When WS$_2$ and Co-W-S catalysts are deposited onto Ti/n$^+$p-Si, their V$_{on}$s shift substantially to more positive potentials than those without Ti buffer layer. The Co-W-S/Ti/n$^+$p-Si has the best PEC performance. A V$_{on}$ of 0.36 V$_{RHE}$ and a J$_0$ of 30.4 mA/cm^2 were obtained under simulated AM1.5 G illumination (100 mW/cm^2). In Fig. S12, we compared the η of the Co-W-S catalyst decorated n$^+$p-Si photocathode with and without the Ti buffer layer. A maximum η of 4.0% was obtained at 0.19 V$_{RHE}$ for the Co-W-S/Ti/n$^+$p-Si electrode, compared with 2.8% for the corresponding Co-W-S/n$^+$p-Si. This demonstrates that the Ti buffer layer plays an important role in enhancing the efficiency of Co-W-S/n$^+$p-Si electrode.

To check the stability of the Co-W-S/Ti/n$^+$p-Si photocathode, long-term PEC measurements were also taken in 1 M HClO$_4$ solution under simulated AM1.5 G illumination (100 mW/cm^2). In Fig. 5c, the PEC-HER current under potentiostatic control at 0 V$_{RHE}$ does not decrease after 6 days of testing, while the stability of Co-W-S/n$^+$p-Si
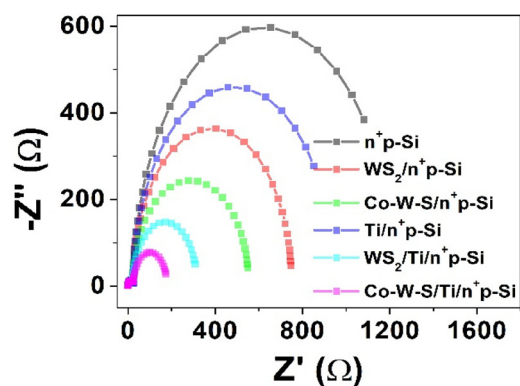
Fig. 6. EIS measurements of n^+p-Si photocathodes with and without WS_2 and Co-W-S catalyst layer and/or Ti buffer layer.

photocathode is only about 45 h, illustrating the high stability of this photocathode. In Fig. S13, we checked the HAADF-STEM image and EDS elemental mappings of Co-W-S/Ti/n^+p-Si sample after 6 days continuous PEC-HER. Compared with the results in Fig. S7, no SiO_2 layer is observed on the interface between catalyst and Si substrate after 6 days of testing, indicating the improved stability of photocathode is originated from the insertion of Ti buffer layer. Note Ti may not be the only buffer layer between Si photocathode and W-Co-S catalyst. Other materials, such as graphene which has superior transmittance, chemical durability and abundant reaction sites for electron transfer, can also be a choice as long as their adhesion to Si is good enough. Finally, we summarized the PEC performance of n^+p-Si photocathodes with various earth abundant electrocatalysts (Table S1). To our delight, both the η and stability of current Co-W-S/Ti/n^+p-Si electrodes are among the highest ones reported so far.

To better understand the different roles of the catalysts and Ti buffer layer, we performed the EIS measurements to elucidate the charge transfer resistances in the different n^+p-Si photocathodes, which were measured at -0.2 V_{RHE} in 1 M $HClO_4$ solution under simulated AM1.5 G illumination. In Fig. 6, each EIS spectra contains two semicircles. The semicircles on the left are nearly the same, indicating that they are assigned to the same n^+p junction. The second semicircles of low frequency range on the right change obviously after the loading of catalysts and Ti buffer layer, indicating that they are related to the front electrode/electrolyte junctions. The EIS data are fitted to the different equivalent circuit for different samples shown in Fig. S14 [44,45].

The charge transfer resistance $R_{ct,1}$ is an indicator of the coupling between the p-Si substrate and the surface n^+-Si doping layer. For all of the samples, $R_{ct,1}$ are between $22.6 \sim 25.3$ Ω, illustrating that the loading of catalysts layer and Ti buffer layer on the n^+p-Si junction hardly change the contact n^+p junction. The results are consistent with the report of Lewis's group that the n^+-layer on p-Si substrate can provide a built-in depletion region which was independent of the semiconductor–liquid junction [46]. When WS_2 and Co-W-S are deposited onto n^+p-Si, the total charge transfer resistances across the Si/catalyst interface are higher than 250 Ω, indicating the mismatch between the catalyst and Si. Interestingly, when the Ti buffer layer is inserted as an interfacial layer between the catalyst and Si, the charge transfer resistances across Si/catalyst (the sum for Si/Ti and Ti/catalyst) dramatically reduces from more than 250 Ω to less than 5 Ω. Obviously, the 8 nm Ti buffer layer can greatly improve the charge transfer rate from Si to catalyst. In addition, the charge transfer resistance from catalyst/electrolyte is also reduced from 555.9 Ω in Co-W-S/n^+p-Si to 183.6 Ω in Co-W-S/Ti/n^+p-Si. This may be originated from the mixture of Ti with the catalyst as illustrated in Fig. 5a. As a result, the total charge transfer resistance (R) across the Si/electrolyte changes significantly, which reduces from 1221 Ω (for pure n^+p-Si), to 774 Ω (for WS_2/n^+p-Si), to 555.9 Ω (for Co-W-S/n^+p-Si), to 324 Ω (for WS_2/

Ti/n^+p-Si), and at last to 183 Ω (for Co-W-S/Ti/n^+p-Si). The Co doping and Ti buffer layer both contribute to the smaller resistances for charge transfer and faster HER rates at the electrode/electrolyte interface.

3. Conclusion

In summary, the Co-W-S/Ti/n^+p-Si photocathode presented herein reveals good PEC-HER performance and impressive operation durability for solar hydrogen production. An ultrathin and homogeneous Co-W-S catalyst layer was produced on Ti/n^+p-Si surface using a cheap wet chemical method, leading to more active sites for PEC reaction than the pure WS_2 catalyst. Simultaneously, the inserted Ti buffer layer played an essential role in protecting Si surface and reducing resistances of charge transfer on the electrode/electrolyte interface. 4.0% η and 6 days stability were finally achieved. This study describes the significant potential for designing high-performance and stable Si photocathodes by integrating Si with noble metal-free catalysts and interfacial layer, which are desirable for energy conversion technologies.

4. Experimental section

4.1. Fabrication of n^+p-Si and Ti/n^+p-Si

Single-crystalline p-Si wafers ($156 \times 156 \times 0.18$ mm^3, $1 - 3$ Ω cm specific resistance) were used for this work. The pyramid surface texture was produced by chemical etching in a solution of KOH and IPA at 78 °C. Then, a n^+ emitter layer (~ 150 nm in thickness) was fabricated on the electrode surface using thermal diffusion of $POCl_4$ at 1000 °C. Bottom electrodes were screen-printed onto the rear surface. After drying the screen-printed samples at 150 °C for 5 min to vaporize the organic solvents in the Al paste, an ohmic contact is formed in an infrared conveyor belt furnace at 900 °C for about 13 s. Then, electrodes were sonicated in 5 wt % HF solution for 30 s to remove the surface native oxide layer and rinsed in deionized water and dried under a stream of N_2. We called such photocathode as n^+p-Si. These n^+p-Si wafers were cut into small pieces 1.5×1.5 cm^2 in size and cleaned by sonication in water, acetone, and ethanol for 5 min each.

Before Ti deposition, Si electrodes were sonicated in 5 wt % HF solution for 30 s to remove the surface native oxide layer again. Ti was sequentially deposited on n^+p-Si *via* electron beam evaporation (E-beam) at a deposition rate of $0.1 - 0.2$ Å/s to form Ti/n^+p-Si. The Ti film thickness of ~ 8 nm was measured using transmission electron microscopy (TEM).

4.2. Fabrication of WS_2 and Co-W-S on the Si and CF substrates

WS_2 catalyst was decorated on n^+p-Si surface through spin-coating and subsequent thermal annealing of the precursor solution. The precursor solution was prepared by adding 34.8 mg of ammonium tetra-thiotungstate (($NH4$)$_2WS_4$) in 5 mL of methanol with the aid of ultra-sonication for 5 min. Native oxide on the Si surface was etched by 5 wt % HF solution for 30 s before catalyst decorating. Specifically, the 50 μL precursor solution was dropped on n^+p-Si samples, and the Si samples were spun at a speed of 600 rpm until methanol was totally evaporated. After drying for several minutes, the samples were moved to a quartz tube mounted in a furnace. The quartz tube was pumped to 133.3 Pa and filled with high purity nitrogen (99.999%). After that, the samples were carried out at different temperature (300 °C, 400 °C and 500 °C) for 2 h under a high purity nitrogen atmosphere with a flow rate of 500 sccm. Afterward, the furnace was naturally cooled to room temperature. This is defined as 1-cycle of deposition. Amount of catalyst on Si surfaces was controlled by the number of deposition cycle. The mass of WS_2 catalyst on Si substrates was estimate to be 0.22 mg/cm^2 after 2-cycle of deposition.

For the fabrication of Co-W-S/n^+p-Si sample, bare cobalt chloride

$(CoCl_2)$ was dissolved in the $(NH4)_2WS_4$ precursor solution. The fabrication procedure of Co-W-S/n^+p-Si was identical to the preparation of WS_2/n^+p-Si photocathode. In order to investigate the Co doping effect, 65 mg, 130 mg and 260 mg $CoCl_2$ were separately added into the $(NH4)_2WS_4$ precursor solution to change the molar ratio of Co/W (1/2, 1/1, 2/1) in Co-W-S catalyst. The fabrication procedures of WS_2/Ti/n^+p-Si and Co-W-S/Ti/n^+p-Si samples were identical to the preparation of WS_2/n^+p-Si and Co-W-S/n^+p-Si photocathodes. The mass of Co-W-S catalyst on Si substrates was estimate to be 0.29 mg/cm^2 after 2-cycle of deposition.

For electrochemical characterization, WS_2 and Co-W-S materials were prepared on CF substrates for electrolysis measurement. All WS_2/CF and Co-W-S/CF fabrication methods were similar to the synthesis steps of WS_2/n^+p-Si and Co-W-S/n^+p-Si. The only difference was using CF as the substrate instead of n^+p-Si.

4.3. Characterization

Advancing contact angle measurements were performed using a SL200 A goniometer (KINO Industry Ltd., USA) for images. The surface morphology of sample surface was analyzed by a Field-Emission scanning electron microscope (SEM) (SU8010, Hitachi). Transmission electron microscope (TEM), scanning transmission electron microscope (STEM), and energy dispersive spectrometer (EDS) characterizations were performed with FEI Talos F200X and Titan FEI Titan^3 G2 60–300 S/TEM. An X-ray diffractometer (XRD, D/MAX-2000PC, Japanese Rigaku) operating under parallel beam mode with Cu Kα radiation was used to characterize the crystal structure. A confocal LabRAM spectrometer (HR800, Jobin Yvon, 532 nm excitation laser) was used to obtain Raman spectra. X-ray photoelectron spectroscopy (XPS) measurements were performed at room temperature using a spectrometer hemispherical analyzer (ESCALAB 250Xi, Thermo) The reflection spectra of the Si samples were measured using a spectrophotometer (Perkin Elmer Lambda 750) in a wavelength range of 300 ~ 1100 nm. UV–vis transmittance spectra of ITO coated glass substrates with and without the decoration of WS_2 and Co-W-S layers were obtained using a UV-VIS-NIR spectrophotometer (UV-3600, Shimadzu).

4.4. PEC measurements

PEC measurements were conducted in a three-electrode cell configuration, using the Si photocathode as working electrode, an Ag/AgCl (3 M KCl) as reference electrode, and a graphite rod as counter electrode. The PEC experiments were performed using an electrochemical workstation (Vertex, Ivium Technologies) in a custom-built Teflon electrolytic cell [13]. For comparison, we checked the PEC J–V of three kinds of Si photocathodes in Fig. 3a by using Pt wire as counter electrode, as shown in Fig. S15. No significant changes are found. The backside of Si photocathode is contacted by a spring-loaded Cu plunger which also presses the working electrode against a Teflon gasket. Thus, only the active area (~ 0.5 cm^2) of the Si photocathode touches the electrolyte. The working electrode was shined through a fused silica window, using simulated AM1.5 G illumination provided by a 300 W Xe lamp (Oriel, Newport Co.) with an AM1.5 G filter (Zhao Jiu Photoelectric Technology co., LTD). During the PEC measurement, the light intensity was carefully maintained at 100 mW/cm^2, measured using an optical power meter (Newport company) just before the light enters into the PEC cell. The electrolyte of electrochemical tests was 1 M $HClO_4$ water solution, which was purged by nitrogen for 30 min. The final potential was translated into the reversible hydrogen electrode (RHE) according to the following equation:

$$E(RHE) = E(Ag/AgCl) + 0.059 V \times pH \qquad (1)$$

where E(Ag/AgCl) = 0.197 V. The performance of the photocathodes was measured using the photocurrent density vs potential (J–V) curves at 50 mV/s in a solution containing 1 M $HClO_4$ (Sinopharm Chemical

Reagent Co., Ltd., Analytical reagent).

For a photocathode, the energy conversion efficiency (η) can be defined as [3]:

$$\eta = \frac{J_{H^+/H_2} \; |V_{op} - E^0| \; FF}{P_{in}} \qquad (2)$$

where V_{op} versus reversible hydrogen electrode (vs. RHE)) is the onset potential measured at a water reduction current density of –1 mA/cm^2; E° is the equilibrium water reduction potential in the 1 M acid electrolyte (pH = 0), which is 0 V vs. RHE; J_{H^+/H_2} (mA/cm^2) is the current density at E°; FF is the fill factor and P_{in} (mW/cm^2) is the incident optical power density.

The EIS of different n^+p-Si photocathodes were measured in a three-electrode configuration using an electrochemical workstation. EIS was performed when the working electrode was biased at a constant potential of $-0.2 V_{RHE}$ under simulated AM1.5 G illumination (100 mW/cm^2), while sweeping the frequency from 0.1 Hz to 100 kHz with an AC amplitude of 10 mV.

To evaluate the stability of Co-W-S/n^+p-Si and Co-W-S/Ti/n^+p-Si photocathodes, a current density vs. time measurement was conducted at constant potential of 0 V_{RHE} for proton reduction in 1 M $HClO_4$ solution under simulated AM1.5 G illumination (100 mW/cm^2). The electrolyte was replaced and the sample was rinsed every 24 h during the stability measurements.

4.5. Electrochemical measurements

Before the electrochemical measurements, as-synthesized WS_2/CF and Co-W-S/CF electrodes were immersed in 1 M $HClO_4$ solution for 12 h. All of the electrochemical measurements were performed using an electrochemical workstation (Vertex, Ivium Technologies) in 1 M $HClO_4$ without solar simulation, with a graphite rod as the counter electrode, an Ag/AgCl (3 M KCl) as the reference electrode and a piece of the as-synthesized WS_2/CF and Co-W-S/CF electrodes were used directly as the working electrode. J–V curve was conducted between -0.2 V and -0.7 V vs. Ag/AgCl electrode at room temperature, with a scan rate of 5 mV/s. To accurately compare the electrocatalytic efficiency of these samples, the ohmic losses throughout the electrochemical system were necessarily corrected. These resistances contributed to the series resistance (R_s), which were obtained by using the electrochemical workstation. The Tafel slopes of different samples stemmed from their corresponding J–V curves. The potential losses were calculated by multiplying the current density of the electrocatalyst material with R_s value based on Ohm's law. The Tafel slope can be calculated by the Tafel equation ($V_{op} = b \log (j) + a$, where j, V_{op}, and b represent the current density, overpotential, and Tafel slope, respectively). Electrochemical impedance spectroscopy (EIS) was performed at a potential of $-0.34 V_{RHE}$ in the dark in a frequency range from 0.1 Hz to 10 kHz with an AC amplitude of 10 mV.

Appendix A. Supplementary data

Supplementary material related to this article can be found, in the online version, at doi:https://doi.org/10.1016/j.apcatb.2018.05.083.

References

[1] K. Sun, S.H. Shen, Y.Q. Liang, P.E. Burrows, S.S. Mao, D.L. Wang, Chem. Rev. 114 (2014) 8662–8719.

[2] I. Roger, M.A. Shipman, M.D. Symes, Nat. Rev. Chem. 1 (2017) 1–13.

[3] M.G. Walter, E.L. Warren, J.R. McKone, S.W. Boettcher, Q.X. Mi, E.A. Santori, N.S. Lewis, Chem. Rev. 110 (2010) 6446–6473.

[4] Q. Ding, J. Zhai, M. Cabán-Acevedo, M.J. Shearer, L. Li, H.C. Chang, M.L. Tsai, D. Ma, X. Zhang, R.J. Hamers, Adv. Mater. 27 (2015) 6511–6518.

[5] D.V. Esposito, I. Levin, T.P. Moffat, A.A. Talin, Nat. Mater. 12 (2013) 562–568.

[6] Q. Ding, F. Meng, C.R. English, M. Cabán-Acevedo, M.J. Shearer, D. Liang, A.S. Daniel, R.J. Hamers, S. Jin, J. Am. Chem. Soc. 136 (2014) 8504–8507.

[7] J.D. Benck, S.C. Lee, K.D. Fong, J. Kibsgaard, R. Sinclair, T.F. Jaramillo, Adv. Energy Mater. 4 (2014) 1400739.

[8] R.L. Fan, J.W. Min, Y. Li, X.D. Su, S. Zou, X.S. Wang, M.R. Shen, Appl. Phys. Lett. 106 (2015) 213901.

[9] R.L. Fan, W. Dong, L. Fang, F.G. Zheng, X.D. Su, S. Zou, J. Huang, X.S. Wang, M.R. Shen, Appl. Phys. Lett. 106 (2015) 013902.

[10] Y. Xu, B. Zhang, Chem. Soc. Rev. 43 (2014) 2439–2450.

[11] M. Zeng, Y.G. Li, J. Mater. Chem. A 3 (2015) 14942–14962.

[12] Y. Hou, X. Zhuang, X. Feng, Small Methods 1 (2017) 1700090.

[13] R.L. Fan, J. Mao, Z.H. Yin, J.S. Jie, W. Dong, L. Fang, F.G. Zheng, M.R. Shen, ACS Appl. Mater. Interfaces 9 (2017) 6123–6129.

[14] Y. Jung, J. Shen, Y. Liu, J.M. Woods, Y. Sun, J.J. Cha, Nano Lett. 14 (2014) 6842–6849.

[15] J. Kibsgaard, Z. Chen, B.N. Reinecke, T.F. Jaramillo, Nat. Mater. 11 (2012) 963–969.

[16] K. Xu, F. Wang, Z. Wang, X. Zhan, Q. Wang, Z. Cheng, M. Safdar, J. He, ACS Nano 8 (2014) 8468–8476.

[17] X. Shang, J. Chi, S. Lu, B. Dong, X. Li, Y. Liu, K. Yan, W. Gao, Y. Chai, C. Liu, Int. J. Hydrogen Energy 42 (2017) 4165–4173.

[18] Z. Huang, C. Wang, Z. Chen, H. Meng, C. Lv, Z. Chen, R. Han, C. Zhang, ACS Appl. Mater. Interfaces 6 (2014) 10408–10414.

[19] Y. Lei, S. Pakhira, K. Fujisawa, X. Wang, O.O. Iyiola, N.P. López, A.L. Elías, L.P. Rajukumar, C. Zhou, B. Kabius, N. Alem, M. Endo, R. Lv, J.L. Mendoza-Cortes, M. Terrones, ACS Nano 11 (2017) 5103–5112.

[20] F. Wang, P. He, Y. Li, T.A. Shifa, Y. Deng, K. Liu, Q. Wang, F. Wang, Y. Wen, Z. Wang, X. Zhan, L. Sun, J. He, Adv. Funct. Mater. 27 (2017) 1605802.

[21] T.A. Shifa, F. Wang, K. Liu, Z. Cheng, K. Xu, Z. Wang, X. Zhan, C. Jiang, J. He, Small 13 (2017) 1603706.

[22] Q. Lu, G.S. Hutchings, W. Yu, Y. Zhou, R.V. Forest, R. Tao, J. Rosen, B.T. Yonemoto, Z. Cao, H. Zheng, J.Q. Xiao, F. Jiao, J.G. Chen, Nat. Commun. 6 (2015) 6567–6574.

[23] J.R. McKone, N.S. Lewis, H.B. Gray, Chem. Mater. 26 (2014) 407–414.

[24] B. Seger, A.B. Laursen, P.C.K. Vesborg, T. Pedersen, O. Hansen, S. Dahl, I. Chorkendorff, Angew. Chem. Int. Ed. 51 (2012) 9128–9131.

[25] M. Cabán-Acevedo, M.L. Stone, J.R. Schmidt, J.G. Thomas, Q. Ding, H. Chang, M. Tsai, J. He, S. Jin, Nat. Mater. 14 (2015) 1245–1251.

[26] C.W. Roske, E.J. Popczun, B. Seger, C.G. Read, T. Pedersen, O. Hansen, P.C.K. Vesborg, B.S. Brunschwig, R.E. Schaak, I. Chorkendorff, H.B. Gray, N.S. Lewis, J. Phys. Chem. Lett. 6 (2015) 1679–1683.

[27] S. Ghoreishi, S. Meshkat, A. Dadkhah, Mater. Res. Bull. 45 (2010) 584–588.

[28] L. Wang, J. Jie, Z. Shao, Q. Zhang, X. Zhang, Y. Wang, Z. Sun, S. Lee, Adv. Funct. Mater. 25 (2015) 2910–2919.

[29] L.L. Feng, G.D. Li, Y. Liu, Y. Wu, H. Chen, Y. Wang, Y.C. Zou, D. Wang, X. Zou, ACS Appl. Mater. Interfaces 7 (2015) 980–988.

[30] M.A. Worsley, S.J. Shin, M.D. Merrill, J. Lenhardt, A.J. Nelson, L.Y. Woo, A.E. Gash, T.F. Baumann, C.A. Orme, ACS Nano 9 (2015) 4698–4705.

[31] X. Wang, X. Gan, T. Hu, K. Fujisawa, Y. Lei, Z. Lin, B.X.Z. Huang, F. Kang, M. Terrones, R. Lv, Adv. Mater. 29 (2017) 1603617.

[32] H. Zhu, J. Zhang, R. Yanzhang, M. Du, Q. Wang, G. Gao, J. Wu, G. Wu, M. Zhang, B. Liu, J. Yao, X. Zhang, Adv. Mater. 27 (2015) 4752–4759.

[33] H. Li, Y. Gao, Y. Shao, Y. Su, X. Wang, Nano Lett. 15 (2015) 6689–6695.

[34] Y. Hou, M. Qiu, G. Nam, M.G. Kim, T. Zhang, K. Liu, X. Zhuang, J. Cho, C. Yuan, X. Feng, Nano Lett. 17 (2017) 4202–4209.

[35] S.M. Sze, M.K. Lee, Semiconductor Devices: Physics and Technology, 3rd ed., Wiley, New York, USA, 2012.

[36] J.K. Nørskova, T. Bligaard, A. Logadottir, J.R. Kitchin, J.G. Chen, S. Pandelov, U. Stimming, J. Electrochem. Soc. 152 (2005) J23–J26.

[37] F. Wang, J. Li, F. Wang, T.A. Shifa, Z. Cheng, Z. Wang, K. Xu, X. Zhan, Q. Wang, Y. Huang, C. Jiang, J. He, Adv. Funct. Mater. 25 (2015) 6077–6083.

[38] J. Wang, W. Cui, Q. Liu, Z. Xing, A.M. Asiri, X. Sun, Adv. Mater. 28 (2016) 215–230.

[39] D. Merki, H. Vrubel, L. Rovelli, S. Fierro, X. Hu, Chem. Sci. 3 (2012) 2515–2525.

[40] L. Feng, M. Fan, Y. Wu, Y. Liu, G. Li, H. Chen, W. Chen, D. Wang, X. Zou, J. Mater. Chem. A 4 (2016) 6860–6867.

[41] H. Li, X. Qian, C. Xu, S. Huang, C. Zhu, X. Jiang, L. Shao, L. Hou, ACS Appl. Mater. Interfaces 9 (2017) 28394–28405.

[42] L. Gao, Y.C. Cui, R.H.J. Vervuurt, D.V. Dam, R.P.J.V. Veldhoven, J.P. Hofmann, A.A. Bol, J.E.M. Haverkort, P.H.L. Notten, E.P.A.M. Bakkers, E.J.M. Hensen, Adv. Funct. Mater. 26 (2016) 679–686.

[43] M.H. Lee, K. Takei, J. Zhang, R. Kapadia, M. Zheng, Y.Z. Chen, J. Nah, T.S. Matthews, Y.L. Chueh, J.W. Ager, A. Javey, Angew. Chem. 124 (2012) 10918–10922.

[44] T. Lopes, L. Andrade, H.A. Ribeiro, A. Mendes, Int. J. Hydrogen Energy 35 (2010) 11601–11608.

[45] H. Zhang, Q. Ding, D. He, H. Liu, W. Liu, Z. Li, B. Yang, X. Zhang, L. Lei, S. Jin, Energy Environ. Sci. 9 (2016) 3113–3119.

[46] S.W. Boettcher, E.L. Warren, M.C. Putnam, E.A. Santori, D. Turner-Evans, M.D. Kelzenberg, M.G. Walter, J.R. McKone, B.S. Brunschwig, H.A. Atwater, N.S. Lewis, J. Am. Chem. Soc. 133 (2011) 1216–1219.